

# Distributions of positron-emitting nuclei in proton and carbon-ion therapy studied with GEANT4

Igor Pshenichnov<sup>1,2</sup>, Igor Mishustin<sup>1,3</sup> and Walter Greiner<sup>1</sup>

<sup>1</sup> Frankfurt Institute for Advanced Studies, Johann Wolfgang Goethe University, 60438 Frankfurt am Main, Germany

<sup>2</sup> Institute for Nuclear Research, Russian Academy of Science, 117312 Moscow, Russia

<sup>3</sup> Kurchatov Institute, Russian Research Center, 123182 Moscow, Russia

## Abstract.

Depth distributions of positron-emitting nuclei in PMMA phantoms are calculated within a Monte Carlo model for Heavy-Ion Therapy (MCHIT) based on the GEANT4 toolkit (version 8.0). The calculated total production rates of  $^{11}\text{C}$ ,  $^{10}\text{C}$  and  $^{15}\text{O}$  nuclei are compared with experimental data and with corresponding results of the FLUKA and POSGEN codes. The distributions of  $e^+$  annihilation points are obtained by simulating radioactive decay of unstable nuclei and transporting positrons in surrounding medium. A finite spatial resolution of the Positron Emission Tomography (PET) is taken into account in a simplified way. Depth distributions of  $\beta^+$ -activity as seen by a PET scanner are calculated and compared to available data for PMMA phantoms. The calculated  $\beta^+$ -activity profiles are in good agreement with PET data for proton and  $^{12}\text{C}$  beams at energies suitable for particle therapy. The MCHIT capability to predict the  $\beta^+$ -activity and dose distributions in tissue-like materials of different chemical composition is demonstrated.

Submitted to: *Phys. Med. Biol.*

PACS numbers: 87.53.Pb, 87.53.Wz, 87.53.Vb

E-mail: pshenich@fias.uni-frankfurt.de

## 1. Introduction

Beams of charged particles, protons and light nuclei, are proved to be very efficient for the radiation therapy of deep-seated solid tumours (Castro *et al* 2004). Their selective and strong impact on a tumour is possible due to a maximum energy deposition at the end of their range in matter (the Bragg peak). According to the statistical data of Particle Therapy Cooperative Group (PTCOG 2006) over 48000 patients were treated worldwide with proton or ion beams by July 2005.

Light nuclei, e.g. carbon ions, have an additional potential advantage compared to protons associated with their enhanced relative biological effectiveness (RBE) (Kraft 2000). Treatment schemes using the carbon-ion irradiation demonstrated good clinical results (Schulz-Ertner *et al* 2004, Tsujii *et al* 2004, Kanai *et al* 2006).

In most cases so far (see PTCOG 2006) the dedicated therapy facilities use either proton or heavy-ion beams. Since 2001, the Hyogo Ion Beam Medical Center (HIBMC)

is the first facility in the world which operates with two types of beams, protons and carbon-ions, in a single location (Hishikawa *et al* 2004, Mayahara *et al* 2005). Several new facilities are planned or under construction in Europe: HIT in Germany (Haberer *et al* 2004, Heeg *et al* 2004), CNAO in Italy (Amaldi 2004), ETOILE in France (Bajard *et al* 2004) and MedAustron in Austria (Griesmayer and Auberger 2004). These particle therapy centres will also have proton and carbon-ion beams on their sites. Each of the two types of beams or their combination will be available for patient treatment.

Successful particle therapy requires thorough treatment planning, which must include optimisation between positive and negative effects of the beam. A required dose of radiation has to be delivered to a tumour while sparing surrounding healthy tissues and organs at risk. The optimisation of doses requires a reliable method for calculating the beam energy deposition in highly heterogeneous human tissues. Up to now, mostly deterministic methods have been used by different groups for dose calculations in hadron therapy, see e.g. Hong *et al* (1996), Krämer *et al* (2000), Jäkel *et al* (2001). However, nowadays a Monte Carlo simulation of particle transport in human body can be used as an alternative method for dose calculations. Increasing power of modern computers makes this method less restrictive in terms of the CPU time (Rogers 2006).

In view of the prospective wide use of both proton and carbon-ion therapy in several medical centres worldwide, one should think of employing common computational tools for proton and ion therapy based on the Monte Carlo approach. We believe that the GEANT4 toolkit (Agostinelli *et al* 2003) is well suited for this purpose. This toolkit was created by an international collaboration of physicists and programmers for basic research in nuclear and particle physics. This is an open-source project based on modern techniques of programming and visualisation. It is capable of simulating a wide range of physical processes in extended media, which makes it useful for applications in medical physics.

The GEANT4 object-oriented toolkit is written in C++ and contains classes and methods which provide the basic functions for simulations (GEANT4-Documents 2006), e.g. handling setup geometry, tracking primary and secondary particles, calculation of their energy loss and energy deposition in matter, run management, visualisation and user interface. On this basis, a specific application can be developed for each particular task. The results on validation of the GEANT4 toolkit for proton therapy (Jiang and Paganetti 2004) and for therapy with electrons and photons (Carrier *et al* 2004, Larsson *et al* 2005) have been presented recently. A GEANT4-based application for emission tomography (GATE) was developed by the Open-GATE collaboration (Jan *et al* 2004) and successfully used in Monte Carlo simulations of commercial PET scanners (Schmidlein *et al* 2006, Lamare *et al* 2006). The GEANT4 toolkit is also used for simulations in brachytherapy (Enger *et al* 2006, Perez-Calatayud *et al* 2006).

In our recent paper (Pshenichnov *et al* 2005) we have made a first attempt to validate the GEANT4 toolkit of version 7.0 (GEANT4-Webpage 2006) for heavy-ion therapy simulations. We have developed a GEANT4-based application for Monte Carlo simulations of Heavy-Ion Therapy (MCHIT). The depth-dose distributions in tissue-like media, calculated within this model, are in a good agreement with experimental data. The relative contribution to the total dose due to secondary neutrons was quantitatively evaluated for proton and ion beams.

In the present work we extend the applicability of the MCHIT model to

calculations of secondary  $\beta^+$ -radioactivity induced by proton and heavy-ion beams in tissue-like media. Currently, the MCHIT application is based on the version 8.0 (with patch 01) of GEANT4 toolkit.

## 2. Dose and range monitoring in particle therapy by positron emission tomography

The main advantage of proton and heavy-ion therapy consists in the possibility to deliver a prescribed dose to a tumour volume while sparing surrounding healthy tissues and organs at risk. This requires thorough verification of the proton and heavy-ion ranges in patient's body. Tissue inhomogeneities and local anatomical changes between fractions of particle therapy may lead to some differences between the actual dose delivered to a patient and the prescribed dose.

Two methods for dose verification in proton and heavy-ion therapy were proposed. In the first method, the beams of  $\beta^+$ -radioactive nuclei  $^{19}\text{Ne}$ ,  $T_{1/2} = 17.22$  s, (Tobias *et al* 1977),  $^{11}\text{C}$ ,  $T_{1/2} = 20.39$  min, (Urakabe *et al* 2001) or  $^{10}\text{C}$ ,  $T_{1/2} = 19.255$  s, (Iseki *et al* 2004) are injected into the patient, fixed in the proper position, just before the therapeutic treatment with the beams of stable nuclei,  $^{20}\text{Ne}$  or  $^{12}\text{C}$ , respectively. However, the practical application of this method is limited by high costs of the radioactive beams.

More frequently another method is used which utilises the fact that  $\beta^+$ -radioactive nuclei are produced in fragmentation reactions taking place in tissues during irradiation with beams of protons or stable nuclei, e.g.  $^{12}\text{C}$ . In proton therapy target fragmentation reactions produce  $^{15}\text{O}$ ,  $T_{1/2} = 122.24$  s, among other fragments. As was early realized (Bennett *et al* 1975, 1978), this can be used for controlling the proton beam localisation in tissues. Later, a similar auto-activation technique, but involving  $^{10}\text{C}$  and  $^{11}\text{C}$  nuclei produced in fragmentation of  $^{12}\text{C}$  projectiles, was proposed for dose monitoring in carbon-ion therapy (Pawelke *et al* 1996, 1997).

Unstable nuclei  $^{10}\text{C}$ ,  $^{11}\text{C}$  and  $^{15}\text{O}$  undergo  $\beta^+$ -decay:  $A(Z, N) \rightarrow A(Z - 1, N + 1) + e^+ + \nu_e$ . Due to the three-body kinematics, the energy released in the transition of a bound proton into a bound neutron is partly carried away also by a neutrino, so that emitted positrons have a continuous energy spectrum. The maximum energy of positrons emitted e.g. by  $^{11}\text{C}$  nucleus is 960 keV with the average energy of 386 keV. Such positrons can travel up to 4 mm in the human body before they stop and annihilate on surrounding electrons:  $e^+e^- \rightarrow \gamma\gamma$ . Due to multiple scattering of positrons, their path in a tissue is far from the straight line, and their average penetration depth is shorter than their actual path. This difference is described by a detour factor (Fernández-Varea *et al* 1996), which is estimated, for example, for 1 MeV electrons or positrons in water as  $\sim 0.5$ . As a result, most of the positrons emitted by  $^{11}\text{C}$  annihilate within  $\sim 2$  mm from their emission point (see also Levin and Hoffman 1999).

In the course of multiple scattering the positrons slow down, so that  $e^+e^-$  annihilation take place practically at rest. Therefore, the angle between the momenta of the emitted photons is close to  $180^\circ$ . They are registered by detectors outside the patient body. Corresponding reconstruction algorithms make possible to obtain the spatial distribution of annihilation points, which should be close to the distribution of positron-emitting nuclei. It is further expected that the spatial distribution of  $\beta^+$ -activity induced by proton and heavy-ion beams is strongly correlated with the corresponding dose distribution. However, there exists no simple way to express the

dose distribution in terms of the  $\beta^+$ -activity distribution.

In practice, the problem is solved in a few steps. First, the  $\beta^+$ -activity distributions are measured in advance in experiments with phantoms for different beam energies and doses. In particular, such measurements have been performed for proton beams in phantoms made of polymethylmethacrylate (PMMA),  $C_5H_8O_2$  or lucite ( $\rho = 1.18 \text{ g/cm}^3$ ) by Oelfke *et al* (1996) and Parodi *et al* (2002). The  $\beta^+$ -activity measurements for  $^{20}\text{Ne}$  beams in PMMA were made by Enghardt *et al* (1992), and later for  $^{12}\text{C}$  beams by Pawelke *et al* (1997), Pönisch *et al* (2004) and Parodi (2004).

Second, the models capable of calculating both the dose and  $\beta^+$ -activity distributions are validated with these data. For example, a phenomenological model for the proton transport incorporating data on isotope production was used by Oelfke *et al* (1996) to calculate the dose and  $\beta^+$ -activity distributions in homogeneous media. Parodi and Enghardt (2000), Parodi *et al* (2002), Pönisch *et al* (2004) simulated the transport of protons and carbon ions in PMMA phantoms with FLUKA and POSGEN codes, respectively. In the present paper we propose to use the GEANT4 toolkit for calculating the dose and  $\beta^+$ -activity distributions.

Third, the dose applied to a patient in a therapeutic treatment can be verified via comparison of the  $\beta^+$ -activity distribution in the patient body with the distribution predicted by the model for the same dose.

### 3. GEANT4 physics models used in MCHIT

We use the version 8.0 (with patch 01) of the GEANT4 toolkit (GEANT4-Webpage 2006) to build a Monte Carlo model for Heavy-Ion Therapy (MCHIT). Currently this model is capable of calculating the three-dimensional distributions of dose and  $\beta^+$ -activity in tissue-like media. In the present study we use homogeneous phantoms represented by a water cube or by a cube made of PMMA. Calculations can also be made for phantoms representing bone, liver or muscle tissues. In simulations the phantom is irradiated by beams of protons or ions with given beam size, emittance, angular convergence/divergence and energy distribution. The phantom material and size, as well as all beam parameters can be set via user interface commands individually for each run.

According to the GEANT4 concept, the set of physical models which are relevant for a particular problem should be activated by the user via a set of commands. A detailed description of physical models included in GEANT4 is given in the Physics Reference Manual (GEANT4-Documents 2006). In order to facilitate this selection, the GEANT4 developers recommend to start either from available examples of previously developed applications, or from the so-called predefined physics lists.

Here we briefly describe the choice of models and main parameters used in our calculations. In MCHIT the energy loss of primary and secondary charged particles due to electromagnetic processes is described via a set of models called 'standard electromagnetic physics'. It accounts for energy loss and straggling due to interaction with atomic electrons as well as multiple Coulomb scattering on atomic nuclei.

At each simulation step, the ionisation energy loss of a charged particle is calculated according to the Bethe-Bloch formula. The mean excitation potential of water molecules was set to 77 eV, i.e. to the value which better describes the set of available data on depth-dose distributions, both for proton and carbon-ion beams, in the range of therapeutic energies of 80 - 330 MeV per nucleon. For PMMA, the

mean excitation potential was set to 68.5 eV, a default value used in GEANT4 for this material.

The bremsstrahlung processes for electrons and positrons were activated in the simulations along with the annihilation process for positrons. For photons, Compton scattering, the conversion into an electron-positron pair and the photoelectric effect were included.

Two kinds of hadronic interactions are considered in the MCHIT model: (a) elastic scattering of hadrons on target protons and nuclei, which dominate at low projectile energies, and (b) inelastic nuclear reactions induced by fast hadrons and nuclei. The model of nucleon-nucleon elastic scattering is based on a parameterisation of experimental data in the energy range of 10-1200 MeV. At higher energies the hadron-nucleus elastic scattering is simulated within the Glauber model (GEANT4-Documents 2006).

Overall probability of hadronic interactions for nucleons and nuclei propagating in the media is determined by the total inelastic cross section for nucleon-nucleus and nucleus-nucleus collisions. Parameterisations by Wellisch and Axen (1996) that best fit experimental data were used to describe the total reaction cross sections in nucleon-nucleus collisions. Systematics by Shen *et al* (1989) was used for the total nucleus-nucleus cross sections.

For inelastic interactions of hadrons two groups of models are available in the GEANT4 toolkit (Agostinelli *et al* 2003): (a) the data-driven models, which are based on the parameterisations of measured cross sections for specific reaction channels, and (b) the theory-driven models, which are based on various theoretical approaches and implemented as Monte Carlo event generators.

In the MCHIT model the inelastic interaction of low-energy (below 20 MeV) nucleons, including radiative neutron capture, were simulated by means of data driven models. Above 20 MeV the exciton-based precompound model was invoked (Agostinelli *et al* 2003).

For hadrons and nuclei with energies above 80A MeV, we have employed the binary cascade model (Folger *et al* 2004). In this case excited nuclear remnants are created after the cascade stage of interaction. Therefore, appropriate models for the de-excitation process should be included in the simulation. The Weisskopf-Ewing model (Weisskopf and Ewing 1940) was used for the description of evaporation of nucleons from nuclei at excitation energies below 3 MeV per nucleon. The Statistical Multifragmentation Model (SMM) by Bondorf *et al* (1995) was used at excitation energies above 3 MeV per nucleon to describe multi-fragment break-up of highly-excited residual nuclei. The SMM includes as its part the Fermi break-up model describing an explosive disintegration of highly-excited light nuclei.

Various unstable nuclei produced in nuclear reactions were followed until their decay, in particular, the  $\beta^+$ -decay leading to the emission of a positron. Within the GEANT4 toolkit such processes are simulated by using the tables of radioactive isotopes with the corresponding decay channels and their probabilities.

#### 4. Production of positron-emitting nuclei by protons and carbon ions

In the case of protons propagating in PMMA the positron-emitting nuclei  $^{11}\text{C}$ ,  $^{10}\text{C}$  and  $^{15}\text{O}$  are created mostly via (p,n) or (p,2n) reactions on  $^{12}\text{C}$  and  $^{16}\text{O}$  nuclei. In this case all the positron-emitting nuclei are fragments of target nuclei which are initially

at rest. In contrast, carbon beams produce  $^{11}\text{C}$  and  $^{10}\text{C}$  nuclei mostly via projectile fragmentation, while  $^{15}\text{O}$  nuclei are produced from the target  $^{16}\text{O}$  nuclei.

The total  $\beta^+$ -activity yields were measured for  $^{11}\text{C}$ ,  $^{10}\text{C}$  and  $^{15}\text{O}$  by Parodi (2004) for protons and carbon ions stopped in PMMA phantoms. Since the half-lives of these nuclides are essentially different and well-known from the literature, one can build a mathematical model describing their decay and the total rate of  $\beta^+$ -activity as a function of time. The measured time-dependence of the total  $\beta^+$ -activity was fitted by Parodi (2004) with the yields of  $^{11}\text{C}$ ,  $^{10}\text{C}$  and  $^{15}\text{O}$  considered as free parameters. The experimental yields of these nuclides obtained in such a way are listed in tables 1 and 2 along with their uncertainties.

Calculational results of the MCHIT model for  $^{11}\text{C}$ ,  $^{10}\text{C}$  and  $^{15}\text{O}$  are listed in tables 1 and 2 for comparison. According to the MCHIT model, the yields of other  $\beta^+$ -emitting nuclei with  $T_{1/2} > 1$  min can be neglected. For example, the yields of  $^{13}\text{N}$ ,  $^{14}\text{O}$ ,  $^{17}\text{F}$  and  $^{18}\text{F}$  nuclei together account for less than 5% of the total yield of  $\beta^+$ -emitters produced by  $\sim 300\text{A}$  MeV  $^{12}\text{C}$  beam in PMMA. The calculations were performed for the PMMA phantoms of the same size (300 mm  $\times$  90 mm  $\times$  90 mm) as used by Parodi (2004) in measurements. The beam profile in the transverse directions was assumed to be a Gaussian with the FWHM of 10 mm, while the beam energy spread was taken with the FWHM of 0.2%.

The results of the FLUKA and POSGEN codes were reported by Parodi (2004) for several beam energies. Some of them are listed in tables 1 and 2, respectively.

**Table 1.** Calculated yields of positron-emitting nuclei (per beam particle, in %) produced by 110, 140 and 175 MeV protons in PMMA phantom. Experimental data and FLUKA results by Parodi (2004) are shown for comparison.

	110 MeV		140 MeV		175 MeV		
	MCHIT	Experiment	MCHIT	Experiment	FLUKA	MCHIT	Experiment
$^{11}\text{C}$	1.83	$2.2 \pm 0.3$	2.64	$3.4 \pm 0.4$	2.67	3.71	$4.7 \pm 0.7$
$^{10}\text{C}$	0.11	$0.09 \pm 0.03$	0.20	$0.15 \pm 0.03$	0.10	0.31	$0.17 \pm 0.06$
$^{15}\text{O}$	0.80	$0.80 \pm 0.15$	1.10	$1.23 \pm 0.18$	1.23	1.54	$1.6 \pm 0.3$

For protons stopped in the PMMA phantom, the yields of  $^{15}\text{O}$  nuclei predicted by the MCHIT model show very good agreement both with the experiment and with the FLUKA results. Since  $^{11}\text{C}$  and  $^{15}\text{O}$  are the most abundant and long-lived nuclides, an accurate description of their yields is crucial for the PET interpretation. As seen from table 1, the agreement between MCHIT results and the experiment is within  $\sim 20\%$  accuracy. As compared with  $^{11}\text{C}$  and  $^{15}\text{O}$  yields, the yield of  $^{10}\text{C}$  is much lower for proton-induced reactions. The MCHIT results for  $^{10}\text{C}$  are in good agreement with the experiment for 110 MeV protons, while for 140 and 175 MeV protons the theory overestimates  $^{10}\text{C}$  yields as compared with the experimental results.

As follows from table 2, the predictions of the POSGEN model for  $^{11}\text{C}$  and  $^{15}\text{O}$  nuclides, reported by Parodi (2004) for 270.55A MeV  $^{12}\text{C}$  ions, are less accurate as compared with the MCHIT model in describing the experimental data at 259.5A MeV. Apparently, more extended benchmarking of the models against each other and experimental data is needed to make a firm conclusion about their performance.

The yields of  $^{10}\text{C}$  nuclei are overestimated by the MCHIT model also for the  $^{12}\text{C}$  beam, in particular, for the most energetic beam of 343.46A MeV. The POSGEN predictions for the beam energy 270.55A MeV are closer to the experimental results

**Table 2.** Calculated yields of positron-emitting nuclei (per beam particle, in %) produced by 212.12A, 259.5A and 343.46A MeV  $^{12}\text{C}$  ions in PMMA phantom. Experimental data at the same beam energies and POSGEN results (calculations for 270.55A MeV  $^{12}\text{C}$ ) by Parodi (2004) are shown for comparison.

	212.12A MeV		259.5A MeV			343.46A MeV	
	MCHIT	Experiment	MCHIT	Experiment	POSGEN	MCHIT	Experiment
$^{11}\text{C}$	11.9	$10.5 \pm 1.3$	16.83	$14.7 \pm 1.6$	26.6	25.25	$19.9 \pm 2.4$
$^{10}\text{C}$	1.97	$0.8 \pm 0.3$	2.79	$1.2 \pm 0.3$	1.96	4.27	$1.5 \pm 0.3$
$^{15}\text{O}$	2.38	$2.1 \pm 0.3$	3.69	$3.1 \pm 0.4$	10.0	6.09	$5.0 \pm 0.4$

obtained at 259.5A MeV. Nevertheless, we conclude that the MCHIT model is able to describe reasonably well the total yields of the most abundant positron-emitting nuclei,  $^{11}\text{C}$  and  $^{15}\text{O}$ , produced by proton and  $^{12}\text{C}$  beams in PMMA.

## 5. Spatial distribution of positron-emitting nuclei

As shown above, the MCHIT model is quite successful in describing the absolute yields of  $\beta^+$ -emitting nuclei. One can now study the spatial distributions of these nuclei. Such distributions were calculated for 110 MeV protons and 212.12A MeV  $^{12}\text{C}$  ions together with the corresponding depth-dose distributions for these beams. The results are presented in figure 1. At these energies, protons and carbon ions have similar ranges in PMMA phantoms. In both cases the Bragg peaks are located at the depth of  $\sim 80$  mm. As demonstrated in the previous section, the contribution from  $^{11}\text{C}$  and  $^{15}\text{O}$  nuclei dominate for both the proton and carbon beams. However, the shapes and the absolute values of corresponding  $\beta^+$ -activity distributions are very different. Protons produce  $^{11}\text{C}$ ,  $^{10}\text{C}$  and  $^{15}\text{O}$  fragments from the target carbon and oxygen nuclei. The cross sections for the  $^{12}\text{C}(\text{p}, \text{pn})^{11}\text{C}$  and  $^{16}\text{O}(\text{p}, \text{pn})^{15}\text{O}$  reactions increase with decreasing proton energy up to 40-50 MeV and then rapidly fall down. For proton energies below 20 MeV there is no neutron emission at all. As shown in figure 1,  $^{11}\text{C}$  and  $^{15}\text{O}$  dominate, and their yields are slowly increasing as the projectile protons slow down. The production of  $^{10}\text{C}$  is significantly suppressed because removal of two neutrons without destroying the remnant is quite improbable. As soon as the proton energy becomes below the neutron emission threshold, the production of  $\beta^+$ -activity is ceased, so that no  $\beta^+$ -emitters are created by protons within  $\sim 1$  cm before the Bragg peak.

In contrast to the proton irradiation, the maximum of  $\beta^+$ -activity produced by carbon ions is located very close to the Bragg peak and thus clearly marks its position. The projectile fragments of interest,  $^{11}\text{C}$  and  $^{10}\text{C}$ , are created in peripheral nucleus-nucleus collisions, and have velocities which are very close to the projectile velocity. At same initial velocity, the ranges of energetic ions in matter  $R$  are proportional to  $A/Z^2$ , where  $A$  and  $Z$  are the ion mass and charge. Therefore, if  $^{11}\text{C}$  and  $^{10}\text{C}$  are created at zero depth, their ranges are shorter as compared to the range of projectile ions:  $R(^{11}\text{C}) \sim 11/12 \times R(^{12}\text{C})$  and  $R(^{10}\text{C}) \sim 10/12 \times R(^{12}\text{C})$ . However, such  $^{11}\text{C}$  and  $^{10}\text{C}$  nuclei can be produced at any depth within the range of primary nuclei, excluding only the last few millimetres of the beam range, where  $^{12}\text{C}$  are not energetic enough for fragmentation. As discussed in details, in particular, by Fiedler *et al* (2006), the spread in production points leads to the spread of stopping points of fragments, as for

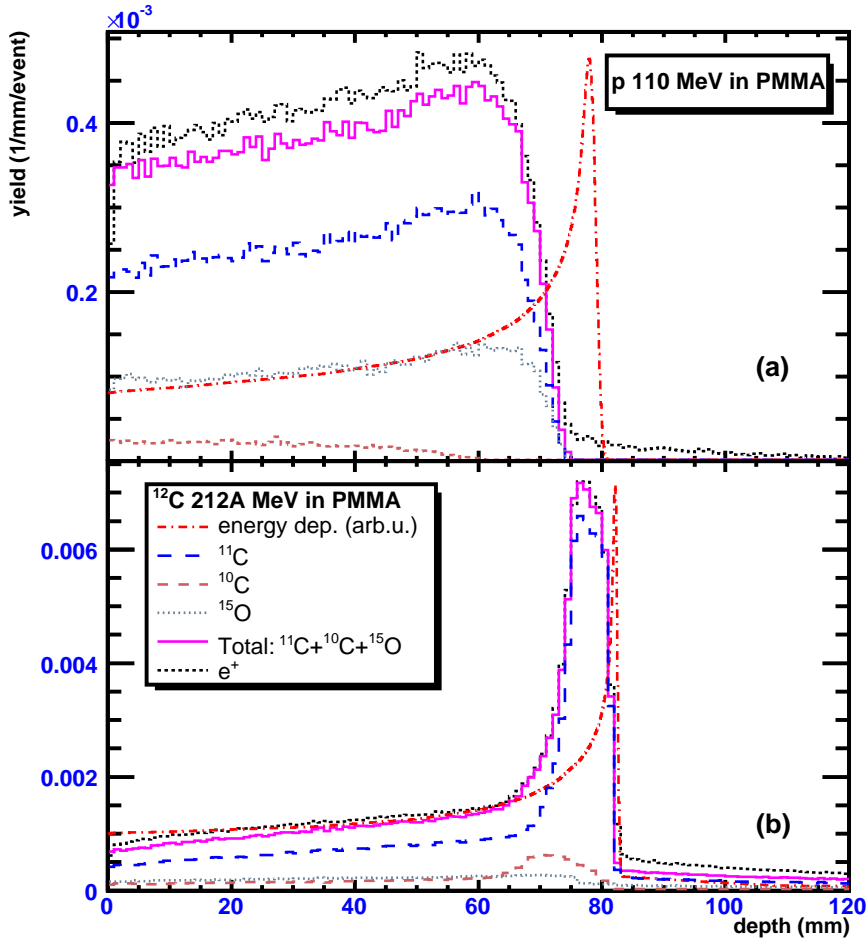


**Figure 1.** Calculated depth-distributions of deposited energy (dash-dotted curves) and  $\beta^+$ -activity (histograms) for (a) 110 MeV protons and (b) 212.12A MeV  $^{12}\text{C}$  nuclei in PMMA phantom. The distributions of  $^{11}\text{C}$ ,  $^{10}\text{C}$  and  $^{15}\text{O}$  nuclei are shown by the long-dashed, dashed and dotted histograms, respectively, and their sum is shown by the solid-line histogram. The distribution of actual  $\text{e}^+$ -annihilation points is shown by the short-dashed histogram.

example, for  $^{11}\text{C}$  fragments this spread can be estimated as  $\Delta x \sim 1/12 \times R(^{12}\text{C})$ .

Despite this spread, all the projectile fragments are stopped before the  $^{12}\text{C}$  Bragg peak. As shown in figure 1, the sharp fall-off in the  $\beta^+$ -activity distribution clearly indicates the position of the Bragg peak. This is a very attractive feature of carbon-ion therapy, which makes possible on-line monitoring of the ions stopping points.

The distribution of  $^{15}\text{O}$  nuclei in  $^{12}\text{C}$  induced reactions looks similar to that for the proton irradiations, since in both cases  $^{15}\text{O}$  nuclei are produced from the target  $^{16}\text{O}$  nuclei. This is why the distribution is quite flat and falls down before the Bragg peak. Strictly speaking, some of  $^{11}\text{C}$ ,  $^{10}\text{C}$  and  $^{15}\text{O}$  nuclei are produced off the target carbon and oxygen nuclei by secondary particles like p,n and  $\alpha$ -particles created in



projectile fragmentation. The contribution of such processes is small, but still visible in figure 1 beyond the Bragg peak, as light secondary particles propagate further.

From the above analysis we see that  $^{11}\text{C}$  fragments are the most suitable nuclei for monitoring the energy deposition in carbon-ion therapy. They have the largest yield and longest life time ( $T_{1/2} = 20.39$  min) as compared with other  $\beta^+$ -emitters. Thus, mostly  $^{11}\text{C}$  nuclei will survive for 10-20 min after stopping, and then emit the positrons.

## 6. Distribution of positron annihilation points as measured by a PET scanner

As explained in section 2, one can measure the depth distribution of  $\beta^+$ -activity via Positron Emission Tomography (PET). Our present study is focused on the ability of the GEANT4 toolkit to describe the production of positron-emitting nuclei rather than on modelling various aspects of PET measurements. As has been already demonstrated by Jan *et al* (2004), Schmidlein *et al* (2006) and Lamare *et al* (2006), the GEANT4 toolkit is very successful in Monte Carlo simulations of commercial PET scanners.

Here we consider only one aspect of the PET monitoring method, i.e. how model predictions are affected by a finite resolution of PET scanners. In our model the PET signal is generated in the following simplified way. First, the decays of all unstable nuclei are simulated at their stopping points. Second, all the emitted positrons are traced up to their annihilation, and, finally, the distribution of  $e^+e^-$ -annihilation points is obtained. It is instructive to note that positrons with energy of a few 100 keV have quite a long mean free path with respect to annihilation in materials like water, namely  $\lambda_{ann} \sim 10$  cm ( $\sigma_{ann} \sim 0.5$  b) at normal water density. Therefore, the annihilation happens only when the positrons have already slowed down.

Third, these distributions are convoluted with Gaussian spreading functions in order to mimic a realistic response of a PET imaging system. We choose the FWHM in the range of 8÷10 mm. Such spatial resolution was reported by Pönisch *et al* (2003) for their 3D PET reconstruction algorithm. Results of our simulations for proton and carbon-ion beams are shown separately in figures 2 and 3.

Since the measured  $\beta^+$ -activity distribution depends on the spatial resolution of the PET scanner, this simple procedure makes possible to compare the calculated  $\beta^+$ -activity profiles with those obtained from experiment, as shown in figures 2 and 3. The distributions of  $e^+$  annihilation points generated with the MCHIT model are shown in figure 2 for 62 and 110 MeV protons in PMMA phantoms. In both cases the distributions are very wide. When the finite PET resolution is taken into account via the convolution of these distributions with a Gaussian of FWHM = 8 mm, only small changes in the shape of the distributions are obtained. Nevertheless, this leads to better description of experimental data by Oelfke *et al* (1996). The agreement with the experiment is very good for 62 MeV protons. On the other hand, some disagreement with the experimental data is found for 110 MeV protons, i.e. the measured distribution is more flat as compared to the calculated one. In figure 3 the MCHIT results are compared with the PET data for carbon ions in PMMA phantoms obtained by Pönisch *et al* (2004) for 212.12A MeV, by Parodi (2004) for 259.5A MeV and by Pawelke *et al* (1997) for 292.5A MeV. Some monitoring devices were placed in front of the PMMA phantoms during measurements while the MCHIT calculations were performed for pure PMMA phantoms without any additional elements. To

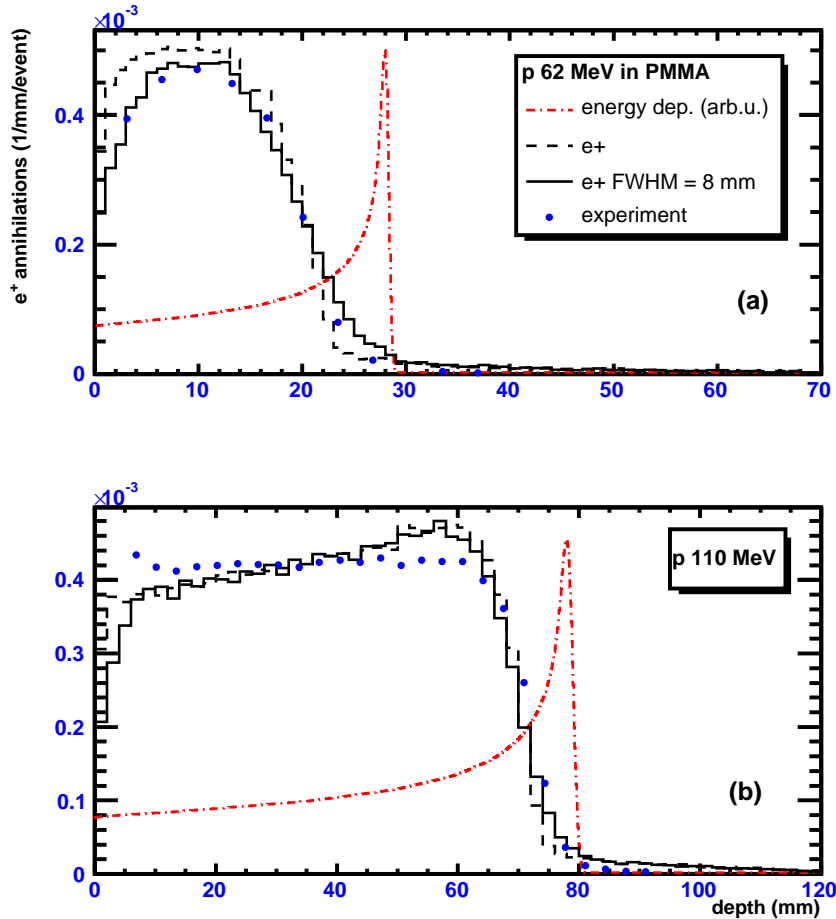


**Figure 2.** Calculated depth-distributions of deposited energy (dash-dotted curve) and positron annihilation points (histograms) for (a) 62 MeV and (b) 100 MeV protons in PMMA phantom. The distribution of actual  $e^+$  annihilation points is shown by the dashed histogram, while the distribution which accounts for a finite spatial PET resolution of FWHM = 8 mm is shown by the solid histogram. Points show experimental data (Oelfke *et al* 1996).

correct for this difference, the experimental data in figure 3 were shifted by 3 - 6 mm to ensure the same position of the Bragg peak in PMMA as reported by Parodi (2004).

For carbon beams, the consideration of the actual PET resolution is crucial for proper description of the experimental data. In this case the actual distribution of  $e^+$  annihilation points consists of a sharp peak on a flat plateau. In order to investigate the effect of the PET scanner resolution, the calculated distributions were convoluted with the Gaussians of FWHM = 8 and 10 mm, resulting in the distributions shown in figure 3. The calculation with FWHM = 8 mm shows a good agreement with the experimental data at 212.12A MeV, while for 259.5A MeV a better agreement is

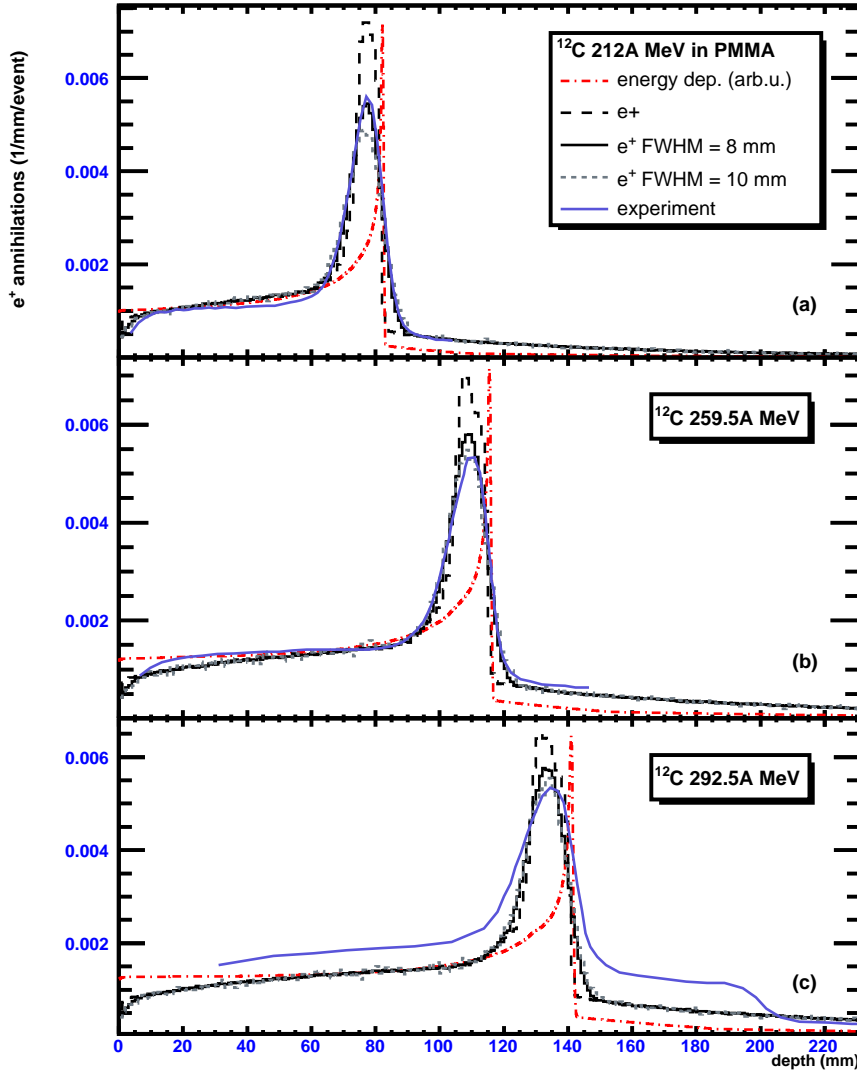


**Figure 3.** Calculated depth-distributions of deposited energy (dash-dotted curve) and positron annihilation points (histograms) for  $^{12}\text{C}$  beam with energy 212A MeV (a), 259.5A MeV (b) and 292.5A MeV (c) in PMMA phantom. The distribution of actual  $e^+$  annihilation points is shown by the long-dashed histogram, while the distributions which account for a finite spatial PET resolution of FWHM = 8 and 10 mm are shown by the solid and short-dashed histograms, respectively. The experimental data are shown by light solid lines: (a) (Pönisch *et al* 2004) (b) (Parodi 2004) and (c) (Pawelke *et al* 1997).

achieved for FWHM = 10 mm. The MCHIT calculations at 292.5A MeV produce a lower plateau as compared with experimental data by Pawelke *et al* (1997). Since the measurements in this case were made promptly after irradiations, the contribution of short-lived isotopes populating the plateau should be bigger compared to the measurements at 212.12A and 259.5A MeV. One can note that the calculations by

Pawelke *et al* (1997) also show the peak-to-plateau ratio, which is higher than found in their measurements.

## 7. Comparison of dose and $\beta^+$ activity distributions in different materials

In order to use the PET method for dose monitoring, the employed calculational tool must well describe both the dose and  $\beta^+$ -activity distributions. As the  $\beta^+$ -activity distributions have been already considered above, we shall study now the corresponding dose distributions calculated with MCHIT, which one can then verify with corresponding experimental data.

The data on dose distributions in PMMA phantoms are rather scarce. Matsufuji *et al* (2003) have performed such measurements for beams of  $^4\text{He}$ ,  $^{12}\text{C}$ ,  $^{20}\text{Ne}$ ,  $^{28}\text{Si}$  and  $^{40}\text{Ar}$  nuclei. In figure 4 the calculated dose distribution for 279.2 A MeV  $^{12}\text{C}$  nuclei in PMMA is compared with the experimental data of Matsufuji *et al* (2003).

As known, the charged particle range in material of a given chemical composition is inversely proportional to the density of electrons, and hence, to the matter density  $\rho$ . In particular, it is quite common to present the depth-dose distributions as functions of the areal density  $x \cdot \rho$ . Then, if  $dE/dx$  is known at one density, it can be easily calculated for other density by rescaling the depth  $x$ . Strictly speaking, this scaling procedure is fully justified only for a given material at various densities. However, one can try to use it also for different tissue-like materials.

In figure 4 the scaling property was used to compare the calculated dose and  $\beta^+$ -activity distributions in water with those in PMMA and in dense bone tissue. The elemental composition of the bone tissue was taken in the following mass fractions: H - 6.4%, C - 27.8%, N - 2.7%, O - 41%, Mg - 0.2%, P - 7%, S - 0.2%, Ca - 14.7%.

In order to get the same position of the Bragg peak, the depth in PMMA and bone were stretched by factors of 1.16 and 1.74, respectively, which are close to the density ratios,  $\rho_{\text{PMMA}}/\rho_{\text{water}} = 1.18$  and  $\rho_{\text{bone}}/\rho_{\text{water}} = 1.85$ . In order to account for the changed bin size, the histograms were rescaled by the inverse factors, 1/1.16 and 1/1.74, respectively. Plotted as functions of water-equivalent depth, the dose and  $\beta^+$ -activity profiles in water and PMMA are in very good agreement with each other despite of the difference in the chemical compositions of PMMA ( $\text{C}_5\text{H}_8\text{O}_2$ ) and water ( $\text{H}_2\text{O}$ ). However, the calculated position of the Bragg peak is  $\sim 4$  mm deeper in water compared to the depth-dose profile measured by Matsufuji *et al* (2003). As discussed by Gudowska *et al* (2004), the position of the Bragg peak in experiment was determined with an accuracy of  $\pm 3$  mm. This discrepancy can be attributed to the uncertainty in the initial energy of the carbon beam. In order to reach agreement with the experimental distributions the data by Matsufuji *et al* (2003) were shifted by 4.2 mm towards the larger depth, see figure 4. This is exactly the same shift, which was used by Gudowska *et al* (2004) to obtain the agreement between the data and the results of their SHIELD-HIT code.

As shown in figure 4, the  $\beta^+$ -activity distributions in water and PMMA can be successfully transformed from one material to another by rescaling. However, this procedure fails for another pair of materials, water and bone tissue. As one can see in figure 4, the scaling transformation does not correctly reproduce the Monte Carlo simulation results for the energy deposition in bone tissue. The-peak-to-plateau ratio for the  $\beta^+$ -activity distribution in bone tissue is lower compared to water due to the difference in their elemental compositions. As explained above, this peak is mainly generated by the  $^{11}\text{C}$  nuclei produced from the projectile  $^{12}\text{C}$  nuclei. These nuclei

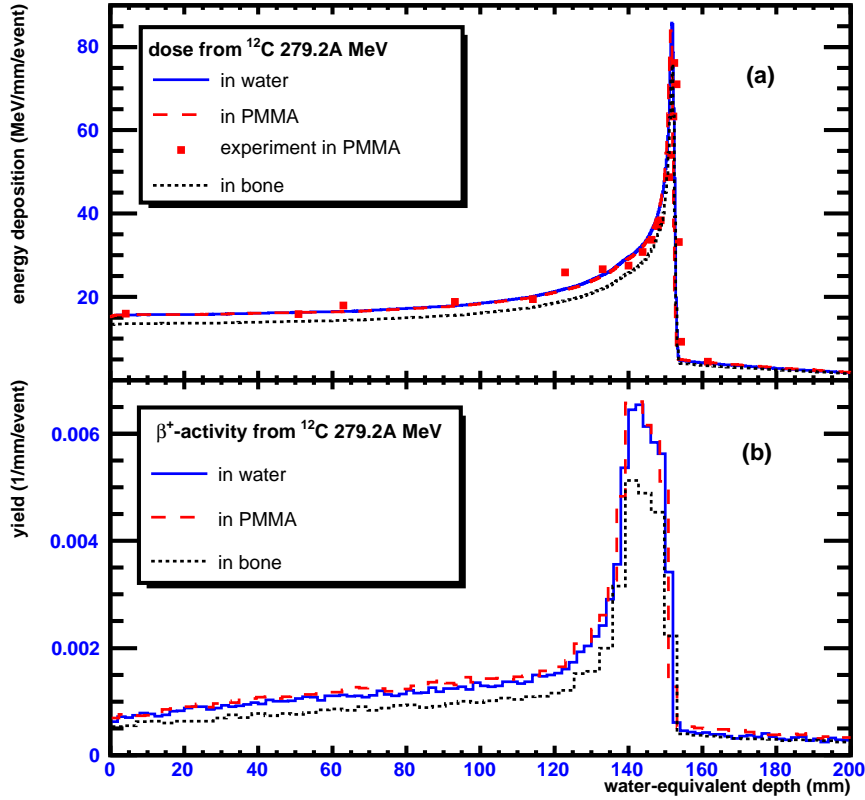


**Figure 4.** (a) Dose distributions as functions of water-equivalent depth calculated for 279.2A MeV  $^{12}\text{C}$  nuclei in water (solid-line histogram), PMMA (dashed histogram) and bone (dotted histogram). Experimental data for depth-dose distributions in PMMA (Matsufuji *et al* 2003) are shown by points. (b) Distributions of positron-emitting nuclei produced in these materials.

are produced less frequently in collisions with target nuclei of bone tissue, which are, on average, more heavy compared with water. In addition, a larger part of the total  $\beta^+$ -activity ( $\sim 10\%$ ) in bone tissue is due to  $^{13}\text{N}$ ,  $^{14}\text{O}$ ,  $^{17}\text{F}$ ,  $^{18}\text{F}$  and  $^{30}\text{P}$  nuclei, which are produced in target fragmentation reactions. This contribution, which also includes the reactions induced by secondary nucleons beyond the Bragg peak, is characterised by a flat depth-distribution.

We believe that after appropriate validation, our Monte Carlo approach can be used for calculating  $\beta^+$ -activity profiles in various materials, as an alternative method to the less accurate scaling transformation. This approach should be especially powerful in the case of strongly inhomogeneous medium as human body where soft tissues are intermittent with voids and bones.

## 8. Conclusion

In the present work the validation of the GEANT4 toolkit for calculations in particle therapy is extended to the  $\beta^+$ -activity distributions induced by proton and  $^{12}\text{C}$  beams. Despite the fact that these  $\beta^+$ -activity distributions differ in shape from the corresponding dose distributions, there exists a strong correlation between them, which can be used for the dose and range monitoring by means of the PET scanners. Since human tissues and organs have various nuclear compositions, only detailed Monte Carlo simulations of proton and carbon-ion therapy are able to account for the differences in  $\beta^+$ -activity distributions for different kinds of tissues, e.g. soft tissues and bones

Our MCHIT model based on the GEANT4 toolkit is able to predict with reasonable accuracy (1) the total yields of  $^{11}\text{C}$  and  $^{15}\text{O}$  nuclei, which are the most abundant  $\beta^+$ -emitters produced by proton and  $^{12}\text{C}$  beams, (2) distributions of  $e^+$  annihilation points as measured by PET scanners with a realistic spatial resolution, (3) the deviations from simple density scaling in the dose and  $\beta^+$ -activity distributions. By this study, the ability of the GEANT4 toolkit to correctly simulate the dose and  $\beta^+$ -activity distributions in the proton and carbon ion therapy has been clearly demonstrated. Therefore, we suggest to use the MCHIT model for realistic calculations of  $\beta^+$ -activity profiles and dose distributions in proton and carbon-ion therapy.

## Acknowledgments

This work was partly supported by Siemens Medical Solutions. We are grateful to Prof. Hermann Requardt for the discussions which stimulated the present study. The discussions with Dr. Thomas Haberer, Prof. Jürgen Debus and Dr. Katia Parodi are gratefully acknowledged.

## References

- Agostinelli S *et al* (GEANT4 Collaboration) 2003 GEANT4: A simulation toolkit *Nucl. Instrum. Meth. A* **506** 250-303
- Amaldi U 2004 CNAO - The Italian Centre for Light-Ion Therapy *Radiother. Oncol.* **73** S191-201
- Bajard M, De Conto J M and Remillieux J 2004 Status of the "ETOILE" project for a French hadrontherapy centre *Radiother. Oncol.* **73** S211-5
- Bennett G W, Goldberg A C, Levine G S, Guthy J, Balsamo J and Archambeau J O 1975 Beam localization via O-15 activation in proton-radiation therapy *Nucl. Instr. Meth.* **125** 333-8
- Bennett G W, Archambeau J O, Archambeau B E, Meltzer J I and Wingate C L 1978 Visualization and transport of positron emission from proton activation in vivo *Science* **200** 1151-3
- Bondorf J P, Botvina A S, Iljinov A S, Mishustin I N and Sneppen K 1995 Statistical multifragmentation of nuclei *Phys. Rept.* **257** 133-221
- Carrier J F, Archambault L, Beaulieu L and Roy R 2004 Validation of GEANT4, an object-oriented Monte Carlo toolkit, for simulations in medical physics *Med. Phys.* **31** 484-92
- Castro J R, Petti P L, Blakely E A and Daftari I K 2004 Particle radiation therapy *Textbook of Radiation Oncology* (Saunders, Elsevier Inc.) ed Leibel S A and Phillips T L pp 1547-68
- Enger S A, Rezaei A, af Rosenschold P M and Lundqvist H 2006 Gadolinium neutron capture brachytherapy (GdNCB), a new treatment method for intravascular brachytherapy *Med. Phys.* **33** 46-51
- Enghardt W, Fromm W D, Geissel H, Keller H, Kraft G, Magel A, Manfrass P, Münzenberg G, Nickel F, Pawelke J, Schardt D, Scheidenberger C and Sobiella M 1992 The spatial-distribution of positron-emitting nuclei generated by relativistic light-ion beams in organic-matter *Phys. Med. Biol.* **37** 2127-31
- Fernández-Varea J M, Andreo P and Tabata T 1996 Detour factors in water and plastic phantoms and their use for range and depth scaling in electron-beam dosimetry *Phys. Med. Biol.* **41** 1119-39

- Fiedler F, Crespo P, Parodi K, Sellesk M, Enghardt W 2006 The feasibility of in-beam PET for therapeutic beams of  $^3\text{He}$  *IEEE Trans. Nucl. Sci.* **53** 2252-9
- Folger G, Ivanchenko V N and Wellisch J P 2004 The Binary Cascade - nucleon-nuclear reactions *Eur. Phys. J. A* **21** 407-17
- GEANT4-Documents 2006 <http://geant4.web.cern.ch/geant4/G4UsersDocuments/Overview/html/>
- GEANT4-Webpage 2006 <http://geant4.web.cern.ch/geant4/>
- Griesmayer E and Auberger T 2004 The status of MedAustron *Radiother. Oncol.* **73** S202-5
- Gudowska I, Sobolevsky N, Andreo P, Belkic D and Brahme A 2004 Ion beam transport in tissue-like media using the Monte Carlo code SHIELD-HIT *Phys. Med. Biol.* **49** 1933-58
- Haberer T, Debus J, Eickhoff H, Jäkel O, Schulz-Ertner D and Weber U 2004 The Heidelberg ion therapy center *Radiother. Oncol.* **73** S186-90
- Heeg P, Eickhoff H and Haberer T 2004 Conception of heavy ion beam therapy at Heidelberg University (HICAT) *Z. Med. Phys.* **14** 17-24
- Hishikawa Y, Oda Y, Mayahara H, Kawaguchi A, Kagawa K, Murakami M and Abe M 2004 Status of the clinical work at Hyogo *Radiother. Oncol.* **73** S38-40
- Hong L, Goitein M, Bucciolini M, Comiskey R, Gottschalk B, Rosenthal S, Serago C and Urie M 1996 A pencil beam algorithm for proton dose calculations *Phys. Med. Biol.* **41** 1305-30
- Iseki Y, Kanai T, Kanazawa M, Kitagawa A, Mizuno H, Tomitani T, Suda M and Urakabe E 2004 Range verification system using positron emitting beams for heavy-ion radiotherapy *Phys. Med. Biol.* **49** 3179-95
- Jäkel O, Krämer M, Karger C P and Debus J 2001 Treatment planning for heavy ion radiotherapy: clinical implementation and application *Phys. Med. Biol.* **46** 1101-16
- Jan S, Santin G, Strul D *et al* 2004 GATE: a simulation toolkit for PET and SPECT *Phys. Med. Biol.* **49** 4543-61
- Jiang H and Paganetti H 2004 Adaptation of GEANT4 to Monte Carlo dose calculations based on CT data *Med. Phys.* **31** 2811-8
- Kanai T, Matsufuji N, Miyamoto T, Mizoe J, Kamada T, Tsuji H, Kato H, Baba M and Tsujii H 2006 Examination of GyE system for HIMAC carbon therapy *Int. J. Radiat. Oncol. Biol. Phys.* **64** 650-6
- Kraft G 2000 Tumor therapy with heavy charged particles *Prog. Part. Nucl. Phys.* **45** S473-544
- Krämer M, Jäkel O, Haberer T, Kraft G, Schardt D and Weber U 2000 Treatment planning for heavy-ion radiotherapy: physical beam model and dose optimization *Phys. Med. Biol.* **45** 3299-317
- Lamare F, Turzo A, Bizais Y, Rest C C and Visvikis D 2006 Validation of a Monte Carlo simulation of the Philips Allegro/GEMINI PET systems using GATE *Phys. Med. Biol.* **51** 943-62
- Larsson S, Svensson R, Gudowska I, Ivanchenko V and Brahme A 2005 Radiation transport calculations for 50 MV photon therapy beam using the Monte Carlo code GEANT4 *Radiat. Prot. Dosimetry.* **115** 503-7
- Levin C S and Hoffman E J 1999 Calculation of positron range and its effect on the fundamental limit of positron emission tomography system spatial resolution *Phys. Med. Biol.* **44** 781-99
- Matsufuji N, Fukumura A, Komori M, Kanai T and Kohno T 2003 Influence of fragment reaction of relativistic heavy charged particles on heavy-ion radiotherapy *Phys. Med. Biol.* **48** 1605-23
- Mayahara H, Oda Y, Kawaguchi A, Kagawa K, Murakami M, Hishikawa Y, Igaki H, Tokuyue K and Abe M 2005 A case of hepatocellular carcinoma initially treated by carbon ions, followed by protons for marginal recurrence with portal thrombus *Radiat. Med.* **23** 513-9
- Oelfke U, Lam G K and Atkins M S 1996 Proton dose monitoring with PET: quantitative studies in Lucite *Phys. Med. Biol.* **41** 177-96
- Parodi K and Enghardt W 2000 Potential application of PET in quality assurance of proton therapy *Phys. Med. Biol.* **45** N151-6
- Parodi K, Enghardt W and Haberer T 2002 In-beam PET measurements of  $\beta^+$  radioactivity induced by proton beams *Phys. Med. Biol.* **47** 21-36
- Parodi K, 2004 On the feasibility of dose quantification with in-beam PET data in radioterapy with  $^{12}\text{C}$  and proton beams 2004, Ph.D. Dissertation, Technische Universität Dresden
- Perez-Calatayud J, Granero D, Ballester F, Crispin V and Van der Laarse R 2006 Technique for routine output verification of Leipzig applicators with a well chamber *Med. Phys.* **33** 16-20
- Pawelke J, Byars L, Enghardt W, Fromm W D, Geissel H, Hasch B G, Lauckner K, Manfrass P, Schardt D and Sobiella M 1996 The investigation of different cameras for in-beam PET imaging *Phys. Med. Biol.* **41** 279-96
- Pawelke J, Enghardt W, Haberer T, Hasch B G, Hinz R, Kramer M, Lauckner K and Sobiella M 1997 In-beam PET imaging for the control of heavy-ion tumour therapy *IEEE Trans. Nucl. Sci.* **44** 1492-8
- Pönisch F, Enghardt W and Lauckner K 2003 Attenuation and scatter correction for in-beam positron

- emission tomography monitoring of tumour irradiations with heavy ions *Phys. Med. Biol.* **48** 2419-36
- Pönisch F, Parodi K, Hasch B G and Enghardt W 2004 The modelling of positron emitter production and PET imaging during carbon ion therapy *Phys. Med. Biol.* **49** 5217-32
- Pshenichnov I, Mishustin I and Greiner W 2005 Neutrons from fragmentation of light nuclei in tissue-like media: a study with the GEANT4 toolkit *Phys. Med. Biol.* **50** 5493-507
- PTCOG 2006 Particle Therapy Cooperative Group Webpage <http://ptcog.web.psi.ch/>
- Rogers D W O 2006 Fifty years of Monte Carlo simulations for medical physics *Phys. Med. Biol.* **51** R287-301
- Schmidtlein C R, Kirov A S, Nehmeh S A, Erdi Y E, Humm J L, Amols H I, Bidaut L M, Ganin A, Stearns C W, McDaniel D L and Hamacher K A 2006 Validation of GATE Monte Carlo simulations of the GE Advance/Discovery LS PET scanners *Med. Phys.* **33** 198-208
- Schulz-Ertner D, Nikoghosyan A, Thilmann C, Haberer T, Jäkel O, Karger C, Kraft G, Wannenmacher M and Debus J 2004 Results of carbon ion radiotherapy in 152 patients *Int. J. Radiat. Oncol. Biol. Phys.* **58** 631-40
- Shen W, Wang B, Feng J, Zhan W, Zhu Y and Feng E 1989 Total reaction cross-section for heavy-ion collisions and its relation to the neutron excess degree of freedom *Nucl. Phys.* **A491** 130-46
- Tobias C A, Benton E V, Capp M P, Chatterjee A, Cruty M R and Henke R P 1977 Particle radiography and autoactivation *Int. J. Radiat. Oncol. Biol. Phys.* **3** 35-44
- Tsuji H, Mizoe J E, Kamada T, Baba M, Kato S, Kato H, Tsuji H, Yamada S, Yasuda S, Ohno T, Yanagi T, Hasegawa A, Sugawara T, Ezawa H, Kandatsu S, Yoshikawa K, Kishimoto R and Miyamoto T 2004 Overview of clinical experiences on carbon ion radiotherapy at NIRS. *Radiother. Oncol.* **73** S41-9
- Urakabe E, Kanai T, Kanazawa M, Kitagawa A, Noda K, Tomitani T, Suda M, Iseki Y, Hanawa K, Sato K, Shimbo M, Mizuno H, Hirata Y, Futami Y, Iwashita Y and Noda A 2001 Spot scanning using radioactive C-11 beams for heavy-ion radiotherapy *Jpn. J. Appl. Phys.* **40** 2540-8
- Weisskopf V E and Ewing D H 1940 On the yield of nuclear reactions with heavy elements *Phys. Rev.* **57** 472-85
- Wellisch H P and Axen D 1996 Total reaction cross section calculations in proton-nucleus scattering *Phys. Rev. C* **54** 1329-32